

Electronic structure investigation of the cubic inverse perovskite Sc_3AlN

Martin Magnuson,^{1,*} Maurizio Mattesini,² Carina Höglund,¹ Igor A. Abrikosov,¹ Jens Birch,¹ and Lars Hultman¹

¹*Department of Physics, Chemistry and Biology (IFM), Linköping University, SE-58183 Linköping, Sweden*

²*Departamento de Física de la Tierra, Astronomía y Astrofísica I, Universidad Complutense de Madrid, E-28040 Madrid, Spain*

(Received 5 September 2008; revised manuscript received 30 October 2008; published 2 December 2008)

The electronic structure and chemical bonding of the recently discovered inverse perovskite Sc_3AlN , in comparison to those of ScN and Sc metal, have been investigated by bulk-sensitive soft-x-ray emission spectroscopy. The measured $\text{Sc } L$, $\text{N } K$, $\text{Al } L_1$, and $\text{Al } L_{2,3}$ emission spectra are compared with calculated spectra using first-principles density-functional theory including dipole transition-matrix elements. The main $\text{Sc } 3d\text{-N } 2p$ and $\text{Sc } 3d\text{-Al } 3p$ chemical bond regions are identified at -4 and -1.4 eV below the Fermi level, respectively. A strongly modified spectral shape of $3s$ states in the $\text{Al } L_{2,3}$ emission from Sc_3AlN in comparison to that for pure Al metal is found, which reflects the $\text{Sc } 3d\text{-Al } 3p$ hybridization observed in the $\text{Al } L_1$ emission. The differences between the electronic structures of Sc_3AlN , ScN , and Sc metal are discussed in relation to the change in the conductivity and elastic properties.

DOI: 10.1103/PhysRevB.78.235102

PACS number(s): 78.70.En, 71.15.Mb, 71.20.-b

I. INTRODUCTION

The early transition-metal nitrides have great technological potential as hard coatings and wide-band-gap semiconductors and possibly for applications in magnetic recording and sensing. However, Sc -based ternary nitride compounds are largely unexplored. The family of compounds with perovskite crystal structure is of scientific interest due to their versatile physical properties such as high Young's modulus, high melting point, colossal magnetoresistance (CMR), and in some cases high-temperature superconductivity (HTS) and ferroelectricity. One of the most stable crystal structures for ternary and multinary compounds is the *cubic* perovskite. Recently, Sc_3AlN , a cubic *inverse* perovskite phase in the ternary Sc-Al-N system, has been synthesized in our laboratory.¹ Presently, there exist only a very limited number of perovskites with cubic inverse perovskite crystal structure, for example, Ti_3AlN (Ref. 2) and Sc_3InN .³ Previous experimental investigations of the occupied and unoccupied electronic states of ternary nitride Ti-Al-N systems include nanolaminated Ti_2AlN .⁴ Recently, a different stable Sc_3GaN cubic inverse perovskite phase was also theoretically predicted.⁵

The cubic inverse perovskite nitrides constitute a relatively unknown branch of the perovskite family. Thus, their electronic structure and chemical bonding have not previously been investigated. The fundamental mechanism for chemical bonding in specific crystal directions leading to certain macroscopic phenomena as high conductivity and elasticity or stiffness needs to be further understood. Detailed knowledge about the character of the electronic states in the interior of inverse perovskites is the key for this understanding. Further, it is important to compare spectra between perovskites and inverse perovskites to understand how the differences in the electronic structure lead to specific physical properties.

The inverse perovskite is a cubic crystal structure with light metal atoms (Al) at the cube corner sites, heavy metal atoms (Sc) at face-centered positions, and the nonmetal atoms (N) in the body-centered position. In effect, the inverse

perovskite is an ordinary perovskite where the heavy metal atoms have exchanged positions with the nonmetal atoms within the unit cell, as shown in Fig. 1.

Here, we investigate the internal electronic structure and the influence of hybridization and chemical bonding between the constituent atoms of the cubic inverse perovskite Sc_3AlN in comparison to those for semiconducting fcc-ScN and hcp-Sc metal, using bulk-sensitive and element-specific soft-x-ray emission (SXE) and soft-x-ray-absorption (SXA) spectroscopy of single-crystal thin-film samples. Experimental and calculated SXA and SXE spectra of pure Sc metal are presented. The SXE technique—with selective excitation energies around the $\text{Sc } 2p$, $\text{N } 1s$, $\text{Al } 2s$, and $\text{Al } 2p$ absorption thresholds—is more bulk sensitive than electron-based spectroscopic techniques. Due to the involvement of both valence and core levels, the corresponding difference in energies of the emission lines, and their dipole selection rules, each kind of atomic element can be probed separately. This enables us to extract both elemental and chemical bonding information of the electronic structure of the valence bands. The SXE and SXA spectra are interpreted in terms of partial density of states (pDOS) weighted by the dipole transition-matrix elements.

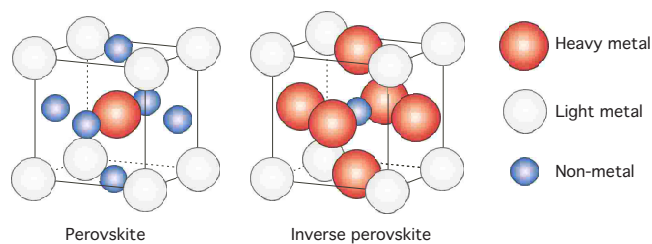


FIG. 1. (Color online) The crystal structures of perovskites and *inverse* perovskites. The heavy metal (Sc) and nonmetal (N , C , or O) atoms have exchanged positions with each other in the inverse perovskite (Sc_3AlN) in comparison to the perovskite structure. The measured (calculated) cubic lattice parameter a is 4.40 Å (4.42 Å) in Sc_3AlN . For comparison, the measured (calculated) lattice parameter for fcc-ScN a is 4.50 Å ($a=4.54$ Å) and those for hcp-Sc are $a=3.31$ and $c=5.27$ Å ($a=3.33$ Å and $c=5.30$ Å).

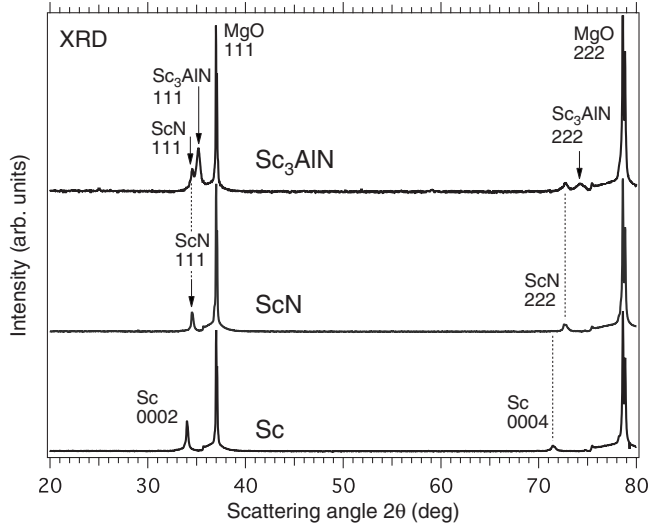


FIG. 2. XRDs from the $\text{Sc}_3\text{AlN}(111)$, $\text{ScN}(111)$, and $\text{Sc}(0001)$ thin-film samples.

II. EXPERIMENTAL

A. Deposition of Sc_3AlN , ScN , and Sc films

Single-crystal stoichiometric $\text{Sc}_3\text{AlN}(111)$, $\text{ScN}(111)$, and $\text{Sc}(0001)$ thin-film samples were grown epitaxially by reactive magnetron sputtering onto polished $\text{MgO}(111)$ substrates, $10 \times 10 \times 0.5 \text{ mm}^3$ in size, at 650, 600, and 280 °C, respectively. The depositions were carried out in an ultrahigh vacuum chamber with a base pressure of 1×10^{-8} Torr from unbalanced type-II magnetrons with 50-mm-diameter Sc and 75-mm-diameter Al targets. Prior to deposition, the substrates were cleaned in ultrasonic baths of trichloroethylene, acetone, and isopropanol, and blown dry in dry N_2 . This was followed by degassing in the chamber for 1 h at 900 °C before ramping down to the deposition temperature. The substrate potential was set to be floating. Prior to the deposition of Sc_3AlN , the substrate was covered with a $\text{ScN}(111)$ seed layer to avoid interdiffusion between the film and the substrate. During deposition, the Ar and N_2 partial pressures were kept at 8.0 mTorr/0.2 mTorr, 8.0 mTorr/0.3 mTorr, and 5.0 mTorr/0 mTorr for Sc_3AlN , ScN , and Sc , respectively, while the Sc and Al magnetron powers were set to 250 W/70 W, 200 W/0 W, and 100 W/0 W, respectively. The thicknesses of the Sc_3AlN , ScN , and Sc films were 1750, 200, and 200 nm, respectively.¹ The crystal structure was characterized with $\theta/2\theta$ x-ray diffraction (XRD) scans in a Philips Bragg-Brentano diffractometer using $\text{Cu } K\alpha$ radiation shown in Fig. 2.

B. X-ray emission and absorption measurements

The SXE and SXA measurements were performed at the undulator beamline I511-3 at MAX II (MAX-laboratory National Laboratory, Lund University, Sweden), comprising a 49-pole undulator and a modified SX-700 plane grating monochromator.⁶ The SXE spectra were measured with a high-resolution Rowland-mount grazing-incidence grating spectrometer⁷ with a two-dimensional multichannel detector

with a resistive anode readout. The Sc L and N K SXE spectra were recorded using a spherical grating with 1200 lines/mm of 5 m radius in the first order of diffraction. The Al L_1 and $L_{2,3}$ spectra were recorded using a grating with 300 lines/mm, of 3 m radius in the first order of diffraction. The SXA spectra at the Sc $2p$ and N $1s$ edges were measured at normal incidence with 0.08 eV resolution using total electron yield (TEY) and total fluorescence yield (TFY), simultaneously. During the Sc L -N K , Al L_1 , and $L_{2,3}$ SXE measurements, the resolutions of the beamline monochromator were 0.45, 0.2, and 0.1 eV, respectively. The Sc L -N K , Al L_1 , and Al $L_{2,3}$ SXE spectra were recorded with spectrometer resolutions of 0.42, 0.3, and 0.06 eV, respectively. All measurements were performed with a base pressure lower than 5×10^{-9} Torr. In order to minimize self-absorption effects,⁸ the angle of incidence was 20° from the surface plane during the emission measurements. The x-ray photons were detected parallel to the polarization vector of the incoming beam in order to minimize elastic scattering.

III. AB INITIO CALCULATION OF SOFT-X-RAY EMISSION SPECTRA

The SXE spectra were calculated with the WIEN2K code⁹ employing the density-functional^{10,11} augmented plane-wave plus local orbital (APW+lo) computational scheme. The APW+lo method expands the Kohn-Sham orbitals in atomic-like orbitals inside the muffin-tin (MT) atomic spheres and plane waves in the interstitial region. For each particular atomic arrangement (hcp-Sc, fcc-ScN, and sc- Sc_3AlN), the Kohn-Sham equations were solved using the Wu-Cohen generalized gradient approximation (GGA) (Refs. 12 and 13) for the exchange-correlation potential.

In all the analyzed structures we used a muffin-tin radius (R_{MT}) of 2.20 a.u. for both Sc and Al, while for N a value of 1.90 a.u. was fixed. The Sc $1s^2$, $2s^2$, and $2p^6$ states were considered as core states, and they were treated using only the spherical part of the potential. In the same manner we handled the Al $1s^2$ and $2s^2$ states and the N $1s^2$ electrons. Only when calculating the Al $L_{2,3}$ edges we set up the aluminum $2p^6$ semicore electrons as pure core states and used an energy cutoff of -4.5 Ry for separating core from valence states, thus leaving the $3s^2$ and $3p^1$ configurations into the valence shell. For the calculation of the valence part, we considered an expansion of the potential and the charge density into spherical harmonics up to $\ell=4$. The valence wave functions inside the atomic spheres were expanded up to $\ell=10$ partial waves. For Sc s , p , and d local orbitals were added to the APW basis set to improve the convergence of the wave function, while for N and Al only s and p local orbitals were included. In the interstitial region, a plane-wave expansion with $R_{\text{MT}}K_{\text{max}}=8$ was used for all the investigated systems, and the potential and the charge density were Fourier expanded with $G_{\text{max}}=8.5$. The modified tetrahedron method¹⁴ was applied to integrate inside the Brillouin zone (BZ), and a k -point sampling with a $27 \times 27 \times 27$ Monkhorst-Pack¹⁵ mesh in the full BZ was considered as satisfactory for the cubic Sc_3AlN and ScN systems, while for the hexagonal Sc a mesh of $30 \times 30 \times 32$ was used.

Electronic band-structure calculations were carried out using the experimental lattice parameters for hcp-Sc [a

$=3.31 \text{ \AA}$ and $c=5.27 \text{ \AA}$ (Ref. 16)] and fcc-ScN [$a=4.50 \text{ \AA}$ (Ref. 17)]. For the cubic inverse perovskite Sc_3AlN , we optimized the unit-cell volume with the APW+lo method and found a lattice constant of 4.37 \AA , which is in reasonable agreement with the experimental value of $a=4.40 \text{ \AA}$.¹ Theoretical emission spectra were then evaluated at the converged ground-state density by multiplying the angular momentum-projected density of states (DOS) by the transition-matrix elements.¹⁸ The electric-dipole approximation was employed so that only the transitions between the core states with orbital angular momentum ℓ to the $\ell \pm 1$ components of the electronic bands were considered.¹⁹ We previously successfully modeled SXE for other nitrides using the same type of theoretical scheme and obtained excellent agreement with experiment,⁴ giving validity and robustness to the present predictions for the Sc_3AlN system. Finally, in order to interpret the experimental Sc $2p_{3/2,1/2}$ and N $1s$ SXA edges, the same kind of first-principles calculations was performed for the unoccupied states of cubic Sc_3AlN and ScN structures. To account for the effect of the Sc $2p$ and N $1s$ core holes on the unoccupied electronic band states, the excited atom was formally treated as an impurity inside a supercell of dimensions $2 \times 2 \times 2$ and a background charge was used to keep the systems neutral.

IV. RESULTS

A. Sc $L_{2,3}$ and N K x-ray emissions

Figure 3 shows Sc $L_{2,3}$ SXE spectra following the $3d4s \rightarrow 2p_{3/2,1/2}$ dipole transitions of Sc_3AlN (full curves), ScN (dotted curves), and Sc metal (dashed curves) excited at 403.0, 404.8, 407.2, 409.0, and 430.0 eV photon energies. As the occupied valence electronic structure of Sc metal nominally only contains one $3d$ electron, the $2p \rightarrow 3d$ SXA transition is strong and the SXE cross section is weak. SXA measurements (top, right curves) following the $2p_{3/2,1/2} \rightarrow 3d4s$ dipole transitions were used to determine the photon energies of the absorption peak maxima at the Sc $2p_{3/2}$ and $2p_{1/2}$ thresholds (vertical ticks). Note that the SXA spectrum of pure Sc metal (dashed curve) has single $2p_{3/2}$ and $2p_{1/2}$ absorption peaks. However, pure Sc metal is very sensitive to surface oxidation when radiated with x rays and naturally forms Sc_2O_3 and ScN at ambient pressure, which makes experiments relatively demanding in terms of vacuum quality and fast measurements, in particular for the surface-sensitive TEY absorption. Surface oxidation from clean Sc metal was observed and monitored with TEY as a function of time after cleaning as a gradual buildup of $t_{2g}-e_g$ ligand-field split double peaks. In the case of Sc_3AlN and ScN, the double peaks are observed as four narrow empty absorption bands in TEY, which are strongest in the case of Sc_3AlN , indicating a thin surface oxide layer and mostly empty $3d$ states. For Sc_3AlN and ScN, the two low-energy absorption peaks at 403.0 and 404.8 eV (1.75 eV $t_{2g}-e_g$ ligand-field splitting) are associated with the empty $2p_{3/2}$ core shell, while the two high-energy peaks are associated with the empty $2p_{1/2}$ core shell.

The SXE spectra (to the left in Fig. 3) of Sc_3AlN and ScN are dominated by the N $2p \rightarrow 1s$ emission, while the intensity

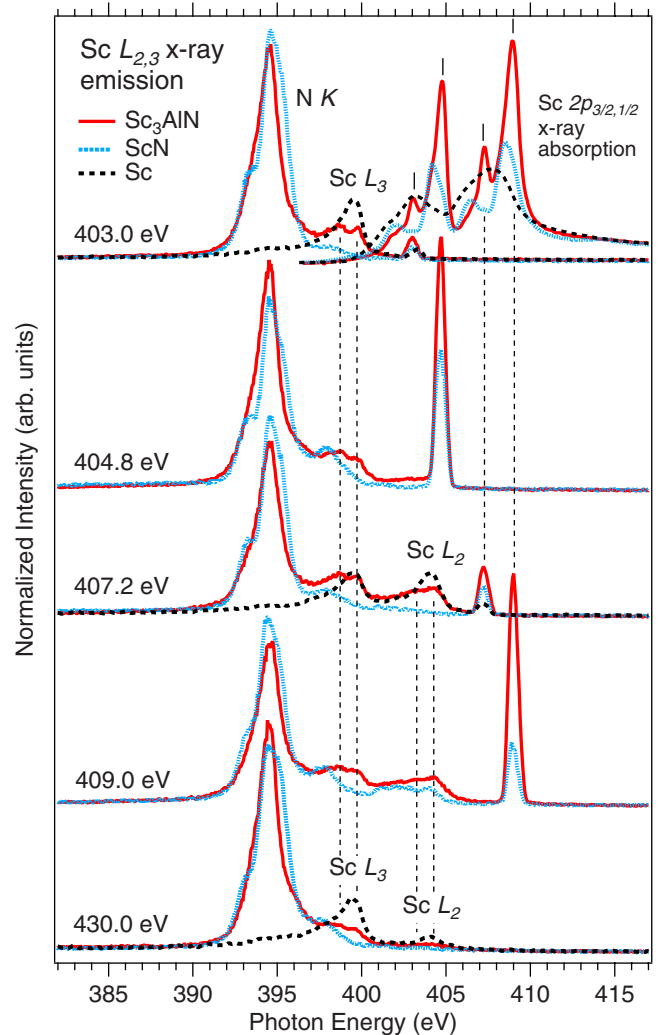


FIG. 3. (Color online) Top right: SXA spectra; left: resonant and nonresonant SXE spectra of the cubic inverse perovskite Sc_3AlN , ScN, and Sc metal. The energy scale has been calibrated with the XPS binding energy of 404.9 eV for Sc $2p_{1/2}$ for ScN (Ref. 20). For comparison of the intensities, the spectra of the different systems were normalized to the calculated charge-density occupations by the integrated areas, while the SXA spectra were normalized by the step edge below and far above the Sc $2p$ absorption thresholds. All spectra were plotted on a photon energy scale. The SXE spectra were resonantly excited at the four Sc $2p$ absorption peak maxima at 403.0, 404.8, 407.2, and 409.0 eV and nonresonant far above the Sc $2p$ and N $1s$ absorption thresholds at 430.0 eV. The excitation energies of the SXE spectra are also indicated by the vertical ticks in the SXA spectra and by the strong elastic recombination peaks determining the total-energy resolution [full width at half maximum (FWHM)=0.65 eV].

of the $2p$ spin-orbit split Sc $3d \rightarrow 2p_{3/2,1/2}$ emission is weaker and appears at higher photon energy. The observed relative Sc/N intensity ratio is generally higher in the SXE spectra of Sc_3AlN than in ScN, which is consistent with the fact that Sc_3AlN contains 10% more Sc than ScN. A low-energy shoulder, more pronounced in ScN than in Sc_3AlN , is observed below the main N K peak. The Rayleigh elastic-scattering peaks of Sc_3AlN and ScN at the resonant excita-

tion energies are strong, which is a signature of localized electron excitations into narrow empty bands. Note that elastic-scattering peaks are not only observed for Sc_3AlN and ScN , but, although weaker, also for pure Sc metal, which is generally not the case for noncorrelated wide-band transition-metal systems in this experimental geometry.⁸ The presence of elastic scattering in pure Sc metal is a signature of localized excitations and electron correlations as normally observed for rare-earth materials²¹ and transition-metal oxides.²² On the other hand, the absence of dispersing resonant *inelastic* x-ray scattering (RIXS) features following below the elastic peaks in all the SXE spectra is a signature of nonionic systems with mainly delocalized electrons. Double-peak features with a splitting of 1.0 eV at constant emission energy (normal emission indicated by the vertical dashed lines in Fig. 3) are observed at both the $\text{Sc } L_3$ and L_2 emissions of Sc_3AlN , but not in ScN and pure Sc metal. These spectral features can be associated with the hybridization with Al as discussed in Sec. IV B.

Although there are indications of electron correlations in all three Sc systems, the normal emission part of the SXE spectra appears as the electrons are mostly delocalized (wide bands), which makes electronic structure calculations suitable for the interpretation, particularly for nonresonant spectra. The observed nonresonant L_3/L_2 branching ratio of the Sc intensity is 3.0 for Sc_3AlN and is somewhat lower than that for Sc metal (3.6), indicating rather good conduction properties for Sc_3AlN . Both for Sc_3AlN and Sc metal, the nonresonant L_3/L_2 branching ratio is higher than the statistical ratio (2:1) due to the additional Coster-Kronig process.⁸ Moreover, the L_3/L_2 ratio is usually significantly higher than 2:1 for conducting systems than for insulators as the Coster-Kronig process is partly quenched by the band gap in insulators.²³

Figure 4 (top) shows SXA spectra (TFY and TEY) together with the nonresonant SXE spectra from the bottom of Fig. 3 (430.0 eV) in comparison to calculated $\text{Sc } L_{2,3}$ and $\text{N } K$ SXE spectra as well as $\text{Sc } 2p$ and $\text{N } 1s$ SXA spectra (bottom) including dipole-projected DOS and appropriate core-hole lifetime broadening of Sc_3AlN , ScN , and Sc metal. Comparing the TEY and TFY measurements, we note that the bulk-sensitive fluorescence yield is more sensitive to the N absorption, while the surface-sensitive electron yield is more sensitive to Sc . The $\text{N } 1s$ absorption peak maximum in TFY is identified at 398.9 eV, which is 4.1 eV below the $\text{Sc } 2p_{3/2}$ absorption maximum (403.0 eV) in TEY.

In the SXE spectra, the main $\text{Sc } 3d$ - $\text{N } 2p$ hybridization region in Sc_3AlN and ScN is identified in the energy region between -3 and -6 eV below E_F with a peak at -4 eV. Due to the 30% lower N content, the experimental Sc_3AlN spectrum is narrower than for ScN . The $\text{N } K$ spectra of Sc_3AlN have a less-pronounced shoulder at -5.5 eV than ScN due to hybridization with the $\text{Al } 3s$ states, while the $\text{Al } 3p$ states mainly hybridize between -1 and -3 eV below E_F . For comparison, the main bonding peak structure is observed at -4.8 eV below E_F in Ti_2AlN .⁴ The peak shift to higher energy from the E_F in Sc_3AlN compared to Ti_2AlN indicates somewhat weaker interaction and bonding, although this is also governed by the relative intensities. The theoretically predicted weak feature due to $\text{Sc } 3d$ - $\text{N } 2s$ hybridization at

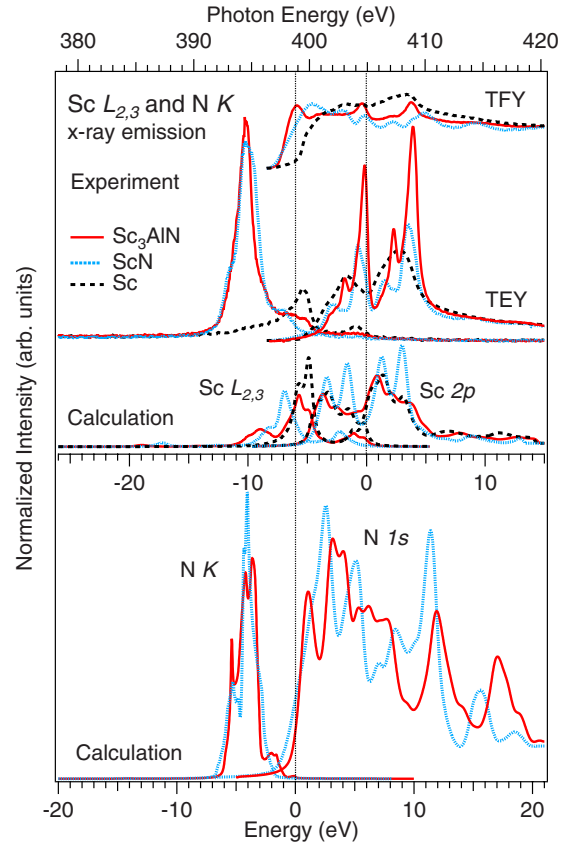


FIG. 4. (Color online) Top: SXA (TFY and TEY) and nonresonant SXE spectra of Sc_3AlN , ScN , and Sc metal excited at 430.0 eV (from Fig. 3). Middle: Calculated $\text{Sc } L_{2,3}$ SXE and $\text{Sc } 2p$ SXA spectra of Sc_3AlN , ScN , and Sc metal. Bottom: Calculated $\text{N } K$ SXE and $\text{N } 1s$ SXA spectra of Sc_3AlN and ScN . Note that the $\text{Sc } L_{2,3}$ and $\text{N } K$ emission partly overlap although the $\text{Sc } L_2$ and $\text{N } K$ Fermi-level energies are separated by 6 eV. The integrated areas of the experimental and calculated spectra of the three systems were normalized to the sum of the calculated $\text{Sc } 3d+4s$ and $\text{N } 2p$ charge occupations of Sc_3AlN ($\text{Sc } s:2.01e$; $\text{Sc } d:0.73e$; and $\text{N } p:3.42e$), fcc- ScN ($\text{Sc } s:2.01e$; $\text{Sc } d:0.66e$; and $\text{N } p:3.41e$), and hcp- Sc metal ($\text{Sc } s:2.03e$ and $\text{Sc } d:0.78e$) where the area of the $\text{Sc } L_2$ component was scaled down by the experimental branching ratio and added to the L_3 component. In the calculated SXA spectra, core-hole correlation effects have also been included in the theory. To account for the difference in the calculated $1s$ core-level energies, the $\text{N } K$ SXE and $\text{N } 1s$ SXA spectra of ScN were shifted by -1.8 eV, relative to the spectra of Sc_3AlN .

-17 eV, however, does not appear experimentally as the $\text{N } 2s$ states are effectively dipole forbidden. For pure Sc metal, a small shoulder observed at 394 eV emission energy (-10 eV below E_F) is not predicted by one-electron theory and may be associated with many-body effects.

Note that for Sc metal, the $3d$ states dominate at the E_F , while for the semiconducting ScN , the $\text{Sc } 3d$ states are at lower energy. From the combination of the spectral edges of the SXA and SXE spectra, the band gap in ScN was estimated to be 1.65 ± 0.5 eV. This is in fairly good agreement with reported indirect band gaps of 0.9 ± 0.1 (Ref. 24) and 1.3 ± 0.3 eV (Ref. 25) in the literature. For Sc_3AlN and Sc metal, the SXE spectra show that the band gap is closed with

Sc $3d$ states at the E_F , indicating good conduction properties, as demonstrated for Sc_3AlN .¹

The observed Sc $2p$ spin-orbit splitting in SXE is 4.70 eV, while it is somewhat smaller in SXA (4.25 eV) and in $2p$ core XPS (4.5 eV). Our calculated *ab initio* value of 4.64 eV is here in good agreement with SXE (4.70 eV), but is somewhat larger than for XPS. The calculated *ab initio* values of the spin-orbit splittings in band-structure calculations are usually underestimated for the early transition metals such as Ti and V and overestimated for the late transition metals such as Ni and Cu.⁸ The reason for the difference in agreement between the experimental and theoretical spin-orbit splittings of different transition metals is not presently known, but must represent effects beyond effective one-electron theory, e.g., many-body effects.

B. Al L_1 and $L_{2,3}$ x-ray emissions

Figure 5 shows Al L_1 (top panel) and Al $L_{2,3}$ (bottom panel) SXE spectra of Sc_3AlN and Al metal,⁴ following the $3p \rightarrow 2s$ and $3s, 3d \rightarrow 2p_{3/2,1/2}$ dipole transitions, respectively. The measurements were made nonresonantly at 140 and 110 eV photon energies. Calculated spectra with the dipole-projected pDOS and appropriate core-hole lifetime broadening are shown by the dotted and dashed curves.

The general agreement between experiment and theory is better for the L_1 emission involving spherically symmetric $2s$ core levels than for the $L_{2,3}$ emission involving $2p$ core levels. The L_1 fluorescence yield is much lower than the $L_{2,3}$ yield, making the L_1 measurements more demanding in terms of extensive beam time. The main Al L_1 emission peak in Sc_3AlN between -1 and -2 eV on the common energy scale is due to Al $3p$ orbitals hybridizing with the Sc $3d$ orbitals. On the contrary, the weak L_1 emission of pure Al metal is very broad and flat without any narrow peak structures in the whole energy region, in agreement with our calculated L_1 spectrum. The very broad spectral structure experimentally observed below -6 eV in the L_1 spectrum of Sc_3AlN is, however, not reproduced in the calculated L_1 spectrum. It can be attributed to hybridization with N $2s$ and Sc $3d$ orbitals at the bottom of the valence band or additional background due to slightly enhanced reflectivity at the low-energy part of the spectrum which becomes visible at long data collection times. Compared to the spectra of Al metal, the spectral structure of Sc_3AlN is focused to a specific energy region (-1.4 eV), as a consequence of Al hybridization with Sc at the top of the valence band and N at lower energy. Bonding Al $3p$ orbitals appear at -1.4 eV below E_F with Sc $3d$ orbitals (and -17 eV with N $2s$ orbitals). Comparing Sc_3AlN to Ti_2AlN ,⁴ the shift of the N $2p$ orbitals to lower energy (from -4.0 to -4.8 eV) implies a shift of the $3d$ pDOS toward lower energy which also affects the spectral distributions of the Al L_1 and $L_{2,3}$ spectra.⁴

The measured Al $L_{2,3}$ SXE spectrum of Sc_3AlN in the lower panel of Fig. 5 is dominated by $3s \rightarrow 2p_{3/2,1/2}$ dipole transitions while additional $3d \rightarrow 2p_{3/2,1/2}$ transitions mainly occur close to the E_F . The electronic structure of the Al atoms is strongly modified by the neighboring atoms. In particular, this is evident when comparing to the Al $L_{2,3}$ spec-

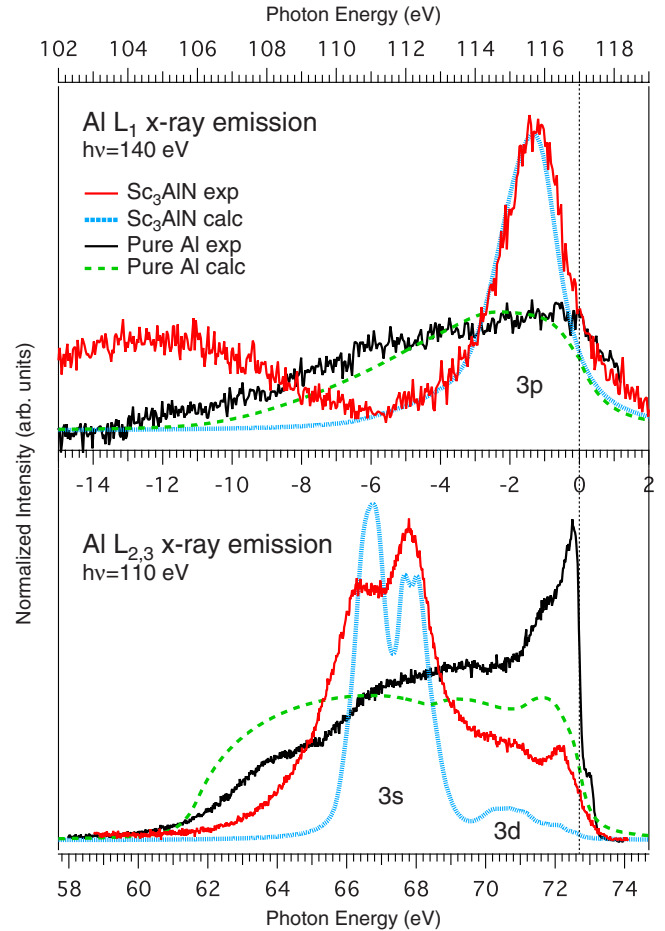


FIG. 5. (Color online) Experimental (full curves) and calculated Al L_1 (dotted curves) and Al $L_{2,3}$ (dashed curves) SXE spectra of Sc_3AlN and single-crystal Al(100). The experimental spectra were excited nonresonantly at 140 and 110 eV, respectively. The vertical dotted line indicates the Fermi level (E_F). A common energy scale with respect to the E_F is indicated in the middle. For comparison of the peak intensities and energy positions, the integrated areas of the experimental and calculated spectra of the two systems were normalized to the calculated Al $3p$ and $3d+3s$ charge occupations of Sc_3AlN ($3p:6.407e$; $3d:0.015e$; and $3s:0.437e$) and pure Al metal ($3p:0.526e$; $3d:0.090e$; and $3s:0.592e$). The area for the L_2 component was scaled down by the experimental branching ratio and added to the L_3 component.

trum of Al metal where a very sharp peak has its maximum at -0.22 eV due to an edge resonance.²⁶ The small shoulder at $+0.24$ eV above E_F in Al metal is due to Al L_2 emission. We find the Al L_3/L_2 branching ratio of Al metal (4.15:1) to be larger than in the case of Sc metal (3.6:1), indicating more metallic properties for Al metal than for Sc metal. The $2p$ spin-orbit splitting is 0.46 eV, slightly larger than our calculated *ab initio* spin-orbit splitting of 0.44 eV. In contrast to the $L_{2,3}$ SXE spectrum of pure Al metal, the Al $L_{2,3}$ spectrum of Sc_3AlN has a strongly modified spectral weight toward lower emission energy. The main peak has its maximum at -5 eV below E_F and a low-energy shoulder at -6 eV, indicating hybridization with the N $2p$ orbitals. We note that the energy positions of the -5 and -6 eV peaks in the calculated spectra are in good agreement with the experiment, while the

intensity distribution is reversed. The peaks at -0.5 and -1.5 eV are due to hybridization with the Sc $3d$ orbitals observed as double structures in Fig. 3 (vertical dashed lines). The Al $2p$ spin-orbit splitting is not resolved in Sc_3AlN . The partly populated $3d$ states are effectively withdrawn from the E_F by charge transfer and form the peak structure at -0.5 eV from hybridization with Sc. For the calculated Al $L_{2,3}$ SXE spectra, the $3s, 3d \rightarrow 2p_{3/2, 1/2}$ matrix elements are important for the spectral functions as the intensity from the pDOS at the top of the valence band is enhanced and at the bottom is reduced. However, the main disagreement between the experimental edge resonance and the one-electron calculation (especially at threshold) can be attributed to many-body effects, addressed in the Mahan–Nozières–De Dominicis (MND) theory of edge singularities.^{27,28}

V. DISCUSSION

Comparing the cubic inverse perovskite crystal structure of Sc_3AlN in Fig. 1 with fcc-ScN, it is clear that the physical properties and the electronic structure are affected by the introduction of the Al atoms. Intuitively, the conductivity should increase since Al metal is a good conductor with very high spectral intensity at the E_F as shown in Fig. 5. The Sc $L_{2,3}$ SXE spectra in Fig. 3 show that the intensity at the E_F is high in Sc_3AlN and Sc metal due to the occupied Sc $3d$ pDOS at the E_F indicating metalliclike properties, while it is withdrawn in ScN below the band gap. For free (delocalized) electrons, the conductivity is proportional to the number of states at the E_F and is largely governed by the metal bonding. Although signs of electron correlations are found in the studied materials, it is useful to compare the trend in the conductivity with the density of states at the E_F : Sc_3AlN , 0.50; ScN, 0.00; Sc, 1.90; TiN, 0.43; Ti_2AlN , 0.41; TiC, 0.12; and Ti_2AlC , 0.34 (in states/eV atom). This trend is in fairly good agreement with experimental values of the resistivity of Sc_3AlN of $0.412 \mu\Omega \text{ m}$,¹ which is slightly higher than for Ti_2AlN films [$0.39 \mu\Omega \text{ m}$ (Ref. 29)] and comparable to that for Ti_2AlC [$0.44 \mu\Omega \text{ m}$ (Ref. 30)]. The resistivity of binary TiN is much lower [$0.13 \mu\Omega \text{ m}$ (Ref. 31)] and for TiC more than an order of magnitude higher [$2.50 \mu\Omega \text{ m}$ (Ref. 32)]. ScN is a hard narrow-band-gap semiconductor (very large resistivity) and pure Sc metal has a resistivity of $0.56 \mu\Omega \text{ m}$.³⁵

From Figs. 3–5, we distinguished three hybridization regions giving rise to the strong Sc $3d$ –N $2p$ bonding at -4 eV below E_F , weaker Sc $3d$ –Al $3p$ bonding at -1.4 eV, and a predicted weak Sc $3d$ –N $2s$ interaction at -17 eV. The Sc $3d$ –N $2p$ covalent bonding and Sc $3d$ –N $2s$ hybridization are both deeper in energy from the E_F than the Sc $3d$ –Al $3p$ hybridization indicating stronger bonding. Strengthening the relatively weak Sc $3d$ –Al $3p$ bonding would increase the stiffness of the material. The measured E modulus of Sc_3AlN is 249 GPa and for ScN it is 356 GPa, which is somewhat lower than in the cases of Ti_2AlN [270

GPa (Ref. 29)] and TiN [449 GPa (Ref. 33)]. By the specific choice of the elements in either a perovskite or an inverse perovskite crystal structure in the design of a material, the physical and mechanical properties can be tailored for specific applications. Further development of future stable cubic inverse perovskite materials include Sc_3GaN . Substitution of Al in Sc_3AlN to Ga in Sc_3GaN would nominally conserve the charge in the sp valence-band electronic structure. However, as in the case of Ge,³⁴ the shallow $3d$ core level, at -19 eV below E_F in Ga will effectively interact with the charge density of the sp valence band which is expected to influence the hybridization and chemical bonding in the material. This will be the subject of further investigations.

VI. CONCLUSIONS

In summary, we have investigated the electronic structure of the cubic inverse perovskite Sc_3AlN in comparison to those of ScN and Sc metal. The combination of bulk-sensitive and element-selective soft-x-ray emission spectroscopy and electronic structure calculations shows that in Sc_3AlN and ScN, the main Sc $3d$ –N $2p$ bond region appear -4 eV below E_F . In Al L_1 emission, a peak observed -1.4 eV below the E_F is due to Al $3p$ states hybridized with Sc $3d$ states in a weaker covalent bonding. Our measured Al $L_{2,3}$ emission in Sc_3AlN as compared to that in pure Al metal shows a significant shift of the main $3s$ intensity from the top of the valence band to hybridization regions at -5 and -6 eV. This signifies an effective transfer of charge from the Al $3d$ orbitals to the N $2p$ and Sc $3d$ orbitals. Absorption and emission measurements of clean Sc metal are presented and the measurements were found to be sensitive to surface oxidation while being irradiated with x rays. The absorption and emission spectra of the investigated Sc systems reveal signs of electron correlations although the main part of the spectra appears as for delocalized and nonionic systems. The revealed hybridization and chemical bond regions for Sc_3AlN and ScN determine the electrical and thermal conductivity and the elastic properties of the materials.

ACKNOWLEDGMENTS

We would like to thank the staff at MAX-laboratory for experimental support. This work was supported by the Swedish Research Council Linnaeus Grant LiLi-NFM, the Göran Gustafsson Foundation for Research in Natural Sciences and Medicine, the Swedish Foundation for Strategic Research (SSF), Strategic Materials Research Center on Materials Science for Nanoscale Surface Engineering (MS²E), and the Swedish Agency for Innovation Systems (VINNOVA) Excellence Center on Functional Nanostructured Materials (FunMat). One of the authors (M. Mattesini) wishes to acknowledge the Spanish Ministry of Science and Technology (MCyT) for financial support through the *Ramón y Cajal* program.

*Corresponding author. Martin.Magnuson@ifm.liu.se

- ¹C. Höglund, J. Birch, M. Beckers, B. Alling, Zs. Czigány, A. Mücklich, and L. Hultman, *Eur. J. Inorg. Chem.* **8**, 1193 (2008).
- ²J. C. Schuster and J. Bauer, *J. Solid State Chem.* **53**, 260 (1984).
- ³M. Kirchner, W. Schnelle, F. R. Wagner, and R. Niewa, *Solid State Sci.* **5**, 1247 (2003).
- ⁴M. Magnuson, M. Mattesini, S. Li, C. Höglund, M. Beckers, L. Hultman, and O. Eriksson, *Phys. Rev. B* **76**, 195127 (2007).
- ⁵A. S. Mikhaylushkin, C. Höglund, J. Birch, Zs. Czigány, L. Hultman, S. I. Simak, B. Alling, and I. A. Abrikosov, *Phys. Rev. B* (to be published).
- ⁶R. Denecke, P. Vaterlein, M. Bassler, N. Wassdahl, S. Butorin, A. Nilsson, J.-E. Rubensson, J. Nordgren, N. Mårtensson, and R. Nyholm, *J. Electron Spectrosc. Relat. Phenom.* **101-103**, 971 (1999).
- ⁷J. Nordgren and R. Nyholm, *Nucl. Instrum. Methods Phys. Res. A* **246**, 242 (1986); J. Nordgren, G. Bray, S. Cramm, R. Nyholm, J.-E. Rubensson, and N. Wassdahl, *Rev. Sci. Instrum.* **60**, 1690 (1989).
- ⁸M. Magnuson, N. Wassdahl, and J. Nordgren, *Phys. Rev. B* **56**, 12238 (1997).
- ⁹P. Blaha, K. Schwarz, G. K. H. Madsen, D. Kvasnicka, and J. Luitz, *WIEN2K, An Augmented Plane Wave Plus Local Orbitals Program for Calculating Crystal Properties* (Karlheinz Schwarz, Technische Universität Wien, Austria, 2001).
- ¹⁰P. Hohenberg and W. Kohn, *Phys. Rev.* **136**, B864 (1964).
- ¹¹W. Kohn and L. J. Sham, *Phys. Rev.* **140**, A1133 (1965).
- ¹²Z. Wu and R. E. Cohen, *Phys. Rev. B* **73**, 235116 (2006).
- ¹³F. Tran, R. Laskowski, P. Blaha, and K. Schwarz, *Phys. Rev. B* **75**, 115131 (2007).
- ¹⁴P. E. Blöchl, O. Jepsen, and O. K. Andersen, *Phys. Rev. B* **49**, 16223 (1994).
- ¹⁵H. J. Monkhorst and J. D. Pack, *Phys. Rev. B* **13**, 5188 (1976).
- ¹⁶F. H. Spedding, A. H. Daane, and K. W. Herrmann, *Acta Crystallogr.* **9**, 559 (1956).
- ¹⁷Z. Gu, J. H. Edgar, J. Pomeroy, M. Kuball, and D. W. Coffey, *J. Mater. Sci.* **15**, 555 (2004).
- ¹⁸J. E. Müller and J. W. Wilkins, *Phys. Rev. B* **29**, 4331 (1984).
- ¹⁹A. Santoni and F. J. Himpsel, *Phys. Rev. B* **43**, 1305 (1991).
- ²⁰D. Gall, R. T. Haasch, N. Finnegan, T.-Y. Lee, C.-S. Shin, E. Sammann, J. E. Greene, and I. Petrov, *Surf. Sci. Spectra* **7**, 167 (2000).
- ²¹M. Magnuson, S. M. Butorin, J. H. Guo, A. Agui, J. Nordgren, H. Ogasawara, A. Kotani, T. Takahashi, and S. Kunii, *Phys. Rev. B* **63**, 075101 (2001).
- ²²M. Magnuson, S. M. Butorin, A. Agui, and J. Nordgren, *J. Phys.: Condens. Matter* **14**, 3669 (2002).
- ²³M. Magnuson, L. C. Duda, S. M. Butorin, P. Kuiper, and J. Nordgren, *Phys. Rev. B* **74**, 172409 (2006).
- ²⁴H. A. Al-Britthen, A. R. Smith, and D. Gall, *Phys. Rev. B* **70**, 045303 (2004).
- ²⁵D. Gall, M. Städele, K. Jarrendahl, I. Petrov, P. Desjardins, R. T. Haasch, T. Y. Lee, and J. E. Greene, *Phys. Rev. B* **63**, 125119 (2001).
- ²⁶U. von Barth and G. Grossmann, *Phys. Scr.* **21**, 580 (1980); V. I. Grebennikov, Yu. A. Babanov, and O. B. Sokolov, *Phys. Status Solidi B* **79**, 423 (1977).
- ²⁷G. D. Mahan, *Phys. Rev.* **163**, 612 (1967).
- ²⁸P. Nozières and C. T. De Dominicis, *Phys. Rev.* **178**, 1097 (1969).
- ²⁹T. Joelsson, A. Horling, J. Birch, and L. Hultman, *Appl. Phys. Lett.* **86**, 111913 (2005).
- ³⁰O. Wilhelmsson, J.-P. Palmquist, T. Nyberg, and U. Jansson, *Appl. Phys. Lett.* **85**, 1066 (2004).
- ³¹J.-E. Sundgren, B.-O. Johansson, A. Rockett, S. A. Barnett, and J. E. Greene, in *Physics and Chemistry of Protective Coatings*, edited by J. E. Greene, W. D. Sproul, and J. A. Thornton (American Institute of Physics, New York, 1986), Ser. 149, p. 95.
- ³²J.-E. Sundgren, B.-O. Johansson, S. E. Karlsson, and H. T. G. Hentzell, *Thin Solid Films* **105**, 367 (1983).
- ³³H. Ljungerantz, M. Odén, L. Hultman, J. E. Greene, and J.-E. Sundgren, *J. Appl. Phys.* **80**, 6725 (1996).
- ³⁴M. Magnuson, O. Wilhelmsson, M. Mattesini, S. Li, R. Ahuja, O. Eriksson, H. Högberg, L. Hultman, and U. Jansson, *Phys. Rev. B* **78**, 035117 (2008).
- ³⁵*CRC Handbook of Chemistry and Physics*, edited by D. R. Lide (CRC, Boca Raton, 2008), 88th ed.